

# Spin resolved bandstructure imaging with a high resolution momentum microscope

Christian Tusche<sup>a,\*</sup>, Alexander Krasnyuk<sup>a</sup>, Jürgen Kirschner<sup>a,b</sup>

<sup>a</sup> Max-Planck-Institut für Mikrostrukturphysik, Weinberg 2, 06120 Halle, Germany

<sup>b</sup> Institut für Physik, Martin-Luther-Universität Halle-Wittenberg, 06099 Halle, Germany

## ARTICLE INFO

### Article history:

Received 3 November 2014

Accepted 22 March 2015

Available online 24 March 2015

### Keywords:

Photoemission

Momentum microscopy

Electronic structure

Spin-orbit coupling

Surface state

Electron spin polarization

## ABSTRACT

We present a spin resolving “momentum microscope” for the high resolution imaging of the momentum distribution of photoelectrons. Measurements of the band structure of a Au(111) single crystal surface demonstrate an energy resolution of  $\Delta E = 12$  meV and a momentum resolution of  $\Delta k_{\parallel} = 0.0049 \text{ \AA}^{-1}$ , measured at the line-width of the spin-orbit split Shockley surface state. The relative accuracy of the  $k_{\parallel}$  measurement in the order of  $10^{-4} \text{ \AA}^{-1}$  reveals a deviation from the ideal two-dimensional free electron gas model of the Shockley surface state, manifested in a threefold radial symmetry. Spin resolution in the full momentum image is obtained by an imaging spin-filter based on low-energy electron diffraction at a Au passivated Ir(100) single crystal. Using working points at 10.5 eV and 11.5 eV scattering energy with a completely reversed asymmetry of  $\pm 60\%$  we demonstrate the efficient mapping of the spin texture of the Au(111) surface state.

© 2015 The Authors. Published by Elsevier B.V. This is an open access article under the CC BY-NC-ND license (<http://creativecommons.org/licenses/by-nc-nd/4.0/>).

## 1. Introduction

Photoelectron spectroscopy has evolved in the past decades as a powerful tool to understand the electronic properties of solid state systems [1]. Specifically, angle-resolved photoelectron spectroscopy (ARPES) aims at the measurement of the valence electronic structure and band-dispersion near the Fermi energy. Experimental work is abundant and covers almost all areas of modern solid-state and surface physics, like strongly correlated electron systems, high temperature superconductivity, and topological insulators [2–7]. While the spin of the electron is decisive in all of these subjects and spin resolved studies regularly provide important new insights into the underlying physics, the spin of the electron is still only poorly accessible. The reason is the inherently low efficiency of electron spin detectors, as the measurement of the spin of a free electron in an “ideal” Stern–Gerlach type filter is not allowed by quantum mechanics.

A primary example that documents the progress in spin- and angle-resolved photoemission, since the pioneering experiments [8–10], is the emission of polarized electrons from a nonmagnetic surface. One such system that additionally requires high energy and angular resolution is the Rashba splitting of the Shockley surface state of Au(111) [11–13]. Beside being a frequent test case for high resolution ARPES, the spin texture of the surface state consists of two concentric rings with a high degree of spin

polarization [14]. Since the first spin resolved measurements [15,16], it became widely used as a reference in spin resolved ARPES, and recently, for understanding peculiar symmetry induced relationships between ground-state- and photoelectron-spin [17–20]. Still, improved experimental and theoretical work reveals limits of the widely accepted picture of the idealized two-dimensional electron gas and the Rashba model [21,22].

On the experimental side, modern hemispherical electron energy analyzers employ a two-dimensional detection scheme to meet the requirements of high resolution spectroscopy. An imaging detector, placed in the open exit plane of the analyzer, measures the emission angle and the energy, simultaneously. Due to the  $\alpha^2$  aberration term inherent to this type of analyzer [23], the ultimate resolution can only be achieved by the restriction to a small volume in phase space. By contrast, most spin detectors used today can only measure one energy- and angular channel at a time [24]. Consequently, a spin-resolved photoemission experiment requires a significant trade-off in resolution. A few recent improvements try to increase the efficiency of the single channel detection, i.e. by exploiting exchange scattering, such that angle resolved experiments in principle became feasible [25,26]. Only recently, two-dimensional spin detection became available for hemispherical analyzers, based on the image conserving reflection of electrons at a crystal surface, resulting in a drastic reduction of measurement time [27].

A different approach for the simultaneous measurement of a two-dimensional photoelectron distribution was introduced by Kotsugi et al. using a photoelectron emission microscope (PEEM)

\* Corresponding author.

[28]. In contrast to a conventional ARPES experiment, all electrons that are emitted from the sample into the complete half space are collected by the accelerating electric field between the sample and the microscope objective lens. In this case, the two image coordinates on the detector do not correspond to emission angles, but to the more meaningful transverse momentum,  $k_{\parallel}$ , of the emitted electron. In this early work, the energy of the photoelectron was fixed to the Fermi edge, limiting the practical use. More recently, a more versatile proof-of-principle of such "momentum microscope" was introduced [29]. This instrument combined a typical PEEM column, as was already used in Ref. [28], with an hemispherical energy analyzer that compensates the  $\alpha^2$  aberration, enabling the fast acquisition of the three-dimensional  $(k_x, k_y, E)$  band dispersion. In particular, the data beyond high-symmetry directions provides valuable input for quantitative theoretical models. For instance, the comprehensive data sets allow us to analyze the effect of band renormalization in photoemission theory [30]. The fixed photoemission geometry gives further direct access to symmetry dependent effects and dichroism [31]. The combination of such a photoelectron microscope with an imaging spin filter already showed that several thousand spin-resolved points can be recorded in an energy filtered microscope image [32,33], making this measurement scheme a promising choice for high-resolution photoemission experiments.

In this paper, we present the first measurements conducted with a new spin-resolving momentum microscope, designed to combine high-resolution momentum resolved bandstructure imaging, with the extremely high efficiency of an imaging spin filter. While the previous generation instruments only had limited resolution in the energy- and momentum coordinates, each being at least one order of magnitude behind that of conventional ARPES setups, we demonstrate that this is not a fundamental limitation of the momentum microscopy principle. We underline this with benchmarking measurements of the electronic structure of a Au (111) single crystal, which represents an ideal test case for the performance of the momentum microscope. Using an imaging spin filter based on the specular reflection of low-energy electrons from a Au/Ir(100) target [34], the spin-texture of the Rashba-split surface state is measured. Our results demonstrate that the Au (111) surface state serves as an ideal reference for the resolution and calibration of an imaging spin filter.

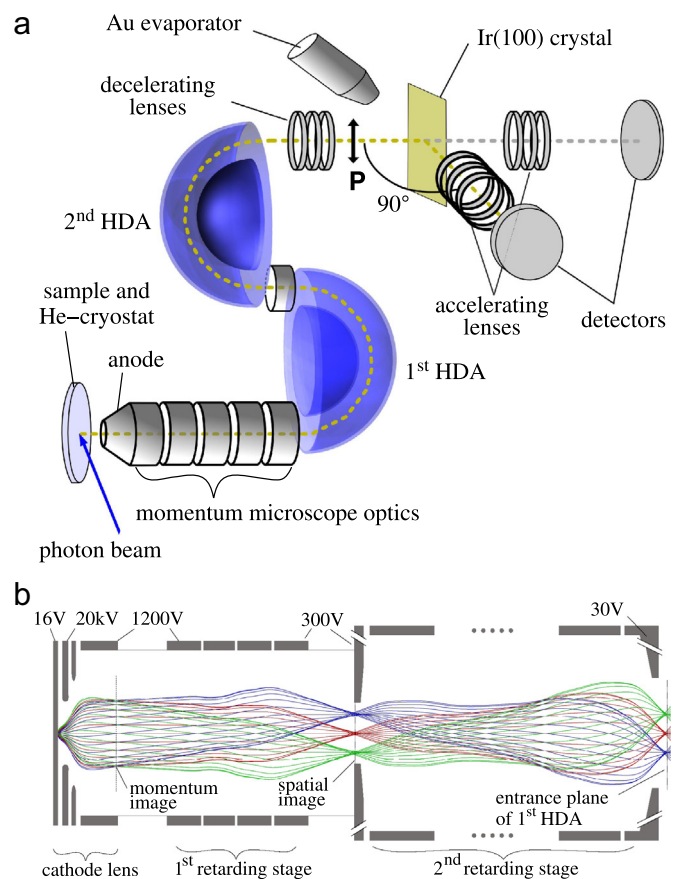
## 2. Description of the momentum microscope

Fig. 1a shows the outline of the momentum microscope system. The most important component is the cathode lens that is formed by the surface of the sample (cathode), kept near ground potential, and the anode at a positive potential. Electrons that are emitted into the complete solid angle above the surface are accelerated towards the anode, and enter the momentum microscope imaging column under a finite angle. This principle allows us to measure emission angles up to  $\pm 90^\circ$ . The maximum value of the parallel momentum that can be found at a given kinetic energy is limited by the vacuum cut-off, determined by the dispersion relation of the free electron

$$k_{\parallel}^{\max} = \beta \cdot \sqrt{E}, \quad (1)$$

where  $\beta = \sqrt{2m_e/\hbar^2}$ , and  $E$  is the kinetic energy of the emitted electron directly above the sample surface.

As the cathode formed by the sample is part of the electron optical system, the mechanical alignment with respect to the anode and the electron optical axis is critical. Therefore, our sample stage is based on a hexapod manipulator that provides alignment in six degrees of freedom. A commercial helium flow cryostat was



**Fig. 1.** (a) Outline of the momentum microscope system, consisting of He-cooled sample stage, imaging electron optics, two hemispherical analyzers, and detection branches for spin-integral and spin-filtered imaging. The Ir(100) crystal can be inserted/retracted after the 2nd HDA. (b) Detail of the momentum microscope optics with schematic arrangement of electrodes and trajectories of 16 eV electrons emitted from the sample.

mounted directly on the hexapod and is moved together with the sample. By measuring the temperature using a silicon diode mounted at the surface of a "dummy" sample, we found a minimum temperature of 18 K.

Energy filtering of the photoelectrons is accomplished by a combination of two hemispherical deflection analyzers (HDAs). Each hemisphere has a mean radius of  $r_0 = 150$  mm and was modified from a commercially available electron spectrometer (PHOIBOS 150, Specs GmbH). Electrons that pass the entrance plane of the first analyzer are deflected in the spherically symmetric  $1/r$  potential, and have the largest energy dispersion after a deflection of  $180^\circ$ . The image obtained in the exit plane of the first HDA is energy dispersed and subject to the  $\alpha^2$  aberration [23]. An effective refocusing of the electron trajectories was described in Ref. [35] by using an electrostatic lens to couple the trajectories to the entrance of the second HDA, such that an effective  $360^\circ$  deflection path is realized. The same principle was also used in previous work [29] and is described in detail in Refs. [36,37]. In short, the solution for a  $360^\circ$  deflection in the spherical  $1/r$  potential is a well-known problem in classical mechanics and leads to closed trajectories (Kepler ellipses). By this symmetry, electron trajectories are refocused in the exit plane of the second HDA to the same spatial and angular coordinates as was the starting point in the entrance plane of the first HDA, transmitting the full image information.

Fig. 1b shows the electron optical principle of the momentum microscope imaging column with simulated electron trajectories between the sample and the entrance plane of the first HDA at a

pass energy of 30 eV, consisting of three major parts: the cathode lens, the first retarding stage and the second retarding stage. Simulations were carried out using the SIMION [38] software. For correct modeling of the cathode lens a sufficiently fine computational mesh has to be chosen in the region between sample and anode [39]. Here, we find converging results for mesh densities larger than 200 points/mm. Fig. 1b shows trajectories for electrons emitted with a kinetic energy of 16 eV. This corresponds to the typical maximum photoelectron energy using the He-I line of a gas discharge source. Trajectories with different color start at the sample surface in a lateral distance of  $-50 \mu\text{m}$ ,  $0$ , and  $+50 \mu\text{m}$  from the optical axis.

Retarding of electrons from the anode potential to the pass energy of the HDA takes place in several steps. The first momentum image is formed at an energy of about 1200 eV in the focal plane of the objective lens, followed by two decelerating lens groups. The first retarding stage is located between the momentum image and the spatial image. The position of the spatial image is kept fixed, such that a movable aperture can be used to select the analyzed area. Finally, the second retarding stage serves three functions: (i) deceleration to the pass energy of the analyzer. (ii) Selection of momentum image or spatial PEEM image. (iii) Variation of the magnification factor (i.e. the field-of-view) for a fixed retarding ratio for PEEM or momentum imaging.

Momentum images are recorded, when a spatial image is placed in the entrance plane of the analyzer. Then, the maximum analyzed sample area is confined by the analyzer slit, and depends on the total real-space magnification,  $M$ , of the intermediate image in the entrance plane. As the analyzer transmits electrons in a limited angular interval  $\pm\alpha_A \approx 3^\circ$ , a direct relation between the momentum field-of-view  $\pm k_{\parallel}^{\text{max}}$  and the total magnification  $M$  can be given. With rotational symmetry, Liouville's theorem requires  $k_{\parallel}^{\text{max}} \cdot d_0 = \sin(\alpha_A) \beta \sqrt{E_{\text{pass}}} \cdot d_A$ , where  $d_0$  and  $d_A$  are the image height at the sample and at the analyzer entrance, respectively. On the right side, the length of the electron momentum vector at the analyzer entrance is  $\beta \sqrt{E_{\text{pass}}}$ . The magnification  $M = d_A/d_0$  then is given by

$$M = \frac{k_{\parallel}^{\text{max}}}{\sin(\alpha_A) \beta \sqrt{E_{\text{pass}}}} \quad (2)$$

In Fig. 1b the total magnification, consisting of the magnification of the objective lens ( $M_O$ ) and the first ( $M_1$ ) and second ( $M_2$ ) retarding stage, is  $M_{\text{total}} = 14$ , with  $M_2 = 1$ . For changing the  $k_{\parallel}$  image diameter,  $M_2$  can be varied between 0.30 and 3.0, under practical conditions. For instance, the measurements discussed in Figs. 3 and 5 correspond to  $M_2 = 1.0$  and  $M_2 = 0.30$ , respectively.

The most critical component, that determines the ultimate  $k_{\parallel}$  resolution, is the cathode lens. The components of the cathode lens are sketched schematically in Fig. 2a, omitting the first retarding stage for simplicity. The cathode is formed by the sample and separated from the anode by the distance  $d_A$ . For the objective lens of the momentum microscope, we choose  $d_A = 4.0 \text{ mm}$ , and a positive high-voltage of  $U_A$  in the range from 20 kV to 35 kV. Trajectories with  $k_{\parallel} = [\pm 2, \pm 1, 0] \text{ \AA}^{-1}$  are focused with equidistant spacing in the momentum image plane. The linear  $k_{\parallel}$  scale in the momentum image plane can be easily understood, as the cathode lens can be described as the combination of a homogeneous accelerating field and an electrostatic imaging lens [40]. The acceleration in the homogeneous field along the optical axis conserves  $k_{\parallel}$  and electrons that are emitted from the surface with the start energy  $E_0$  enter the objective lens under an effective angle  $\alpha'$  with respect to the optical axis

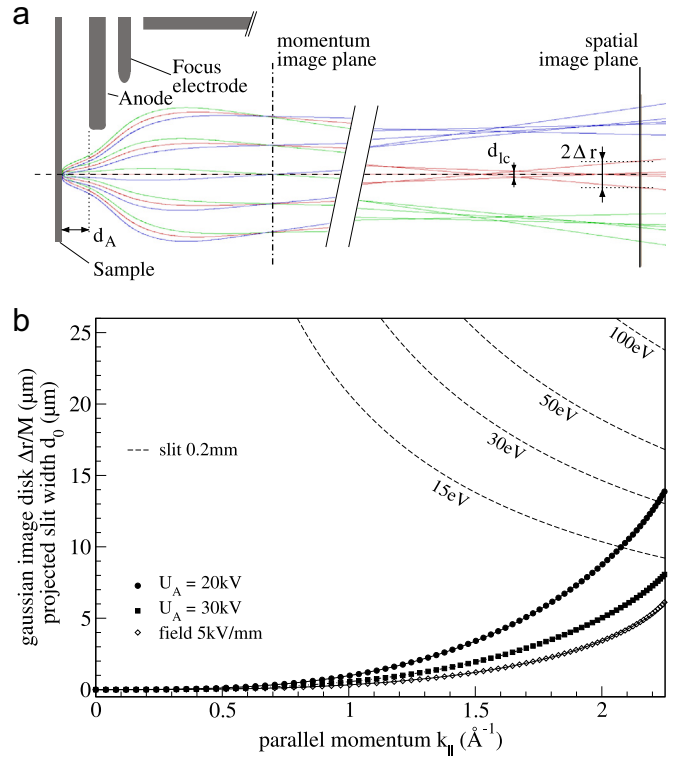


**Fig. 2.** (a) Schematic geometry of the objective lens, consisting of the sample, the anode and two focussing electrodes. Electron trajectories start from an area of  $\pm 50 \mu\text{m}$  at the sample and maximum  $k_{\parallel} = \pm 2 \text{ \AA}^{-1}$ . (b) Transverse displacement of electrons (symbols) in the first gaussian image plane and projected width of the 0.2 mm analyzer slit (dashed lines) for various pass energies as indicated by the labels.

$$\sin(\alpha') = \frac{k_{\parallel}}{\beta \cdot \sqrt{eU_A + E_0}} \quad (3)$$

For a geometrical lens with focal length  $f$ , a beam that enters the lens under the angle  $\alpha'$  will be focused in the momentum image plane in the distance  $r_k = f \cdot \tan(\alpha')$  from the optical axis. When the anode acceleration voltage is large compared to the start kinetic energy of the emitted electron,  $eU_A \gg E_0$ , the effective angle  $\alpha'$  does only depend on the parallel momentum coordinate,  $k_{\parallel}$ , and, with  $\tan(\alpha') \approx \sin(\alpha')$ , the transverse position in the momentum image plane becomes linear in  $k_{\parallel}$ .

Our electron optical simulations show that the aberrations of the retarding- and projection-lenses are negligible compared to those of the objective lens. In Fig. 2a, the spherical aberration in the spatial image plane is most pronounced. Fig. 2b shows the calculated transverse displacement (solid symbols),  $\Delta r$ , normalized to the magnification,  $M_O$ , as a function of the parallel momentum,  $k_{\parallel}$ , that is simultaneously acquired. In first approximation, the spherical aberration depends on the third power of the angle of the electron trajectory with respect to the optical axis [41],  $\Delta r \approx C_5 M_O \alpha'^3$ . In general, higher order terms include the higher uneven exponents to  $\alpha'$ . Here,  $\alpha'$  denotes the finite angle under which the electrons enter the lens [42] (see Eq. (3)). Using Eq. (3) the transverse displacement in the image plane can conveniently be written as

$$\Delta r = C_5^k M k_{\parallel}^3 + C_5^k M k_{\parallel}^5 + O(k_{\parallel}^7) \quad (4)$$

With this representation, the aberration of a cathode lens for a given  $k_{\parallel}$  image radius can be directly compared. Values obtained from the electron optical simulation are summarized in Table 1.

**Table 1**

Aberration coefficients with respect to  $k_{\parallel}$  of the cathode lens as derived from the electron optical simulations displayed in Fig. 2b for 20 eV electrons starting with different  $k_{\parallel}$ .

	Field (kv/mm)	$C_3^k$ ( $\mu\text{m}\cdot\text{\AA}^3$ )	$C_5^k$ ( $\mu\text{m}\cdot\text{\AA}^5$ )
$U_A=20$ kV	5.0	0.955	0.019
$U_A=30$ kV	7.5	0.546	0.011
Hom. field	5.0	0.317	0.016

For the higher anode voltage, both coefficients are reduced, and a larger  $k_{\parallel}$  radius can be imaged. For comparison, open symbols in Fig. 2b show the contribution to the spherical aberration introduced by the acceleration in a homogeneous field of 5 kV/mm. Analytical expressions for  $\Delta r$  can, for instance, be found in Ref. [40]. The direct comparison of the coefficients in Table 1 shows that the third-order term is mainly introduced by the lens, while the contribution to the fifth-order term is mainly due to the accelerating field. As the fifth-order term becomes important at large values of  $k_{\parallel}$ , a high acceleration voltage is preferred in that case.

Dashed lines in Fig. 2b show the projected width  $d_0$  of the 0.2 mm analyzer slit on the sample surface, and illustrates the interplay between spherical aberration and analyzed area. For  $d_0 > \Delta r$ , the disk of least confusion,  $d_{lc}$ , obtained at the optimum focus (see Fig. 2a) fits twice in the slit width, and the momentum information is collected from the selected area. For instance, for the 0.2 mm slit this is fulfilled for all pass energies up to  $k_{\parallel}^{\text{max}} = 2 \text{\AA}^{-1}$ . It is also evident that when a smaller field-of-view is selected by changing the magnification factor, electrons will be collected from a larger area. As both,  $k_{\parallel}^{\text{max}}$  and  $M$ , enter linear in Eq. (2) the total transmission is constant when the momentum image is zoomed in to a smaller field-of-view, as will be demonstrated below for measurements of the Au(111) Shockley surface state. In consequence, image acquisition times are independent of the selected diameter of the momentum image.

An imaging spin-filter, described earlier in Refs. [32,33], is installed at the exit of the second HDA. Electrostatic decelerating and accelerating lenses before and after the scattering target allow the selection of the scattering energy,  $E_{\text{scatt}}$ , of electrons at the target crystal independently of  $E_{\text{pass}}$ , and the projection of the spin-filtered image on the respective detector. In contrast to previous work [32,33], where a W(100) single crystal was used as spin selective mirror, here we use an Ir(100) single crystal, passivated by a pseudomorphic monolayer of Au [34], as outlined below. Spin integrated images are recorded on the direct image detector by retracting the Ir(100) crystal from the electron optical beam path. Images are recorded by a cooled CCD camera from the detector assembly, consisting of a multi-channel-plate (MCP) image intensifier and a 40 mm diameter fluorescent screen.

### 3. Results

The Au(111) single crystal was prepared by repeated cycles of Ar-ion sputtering and annealing at 600 °C. Low energy electron diffraction patterns of the clean surface show the well-known  $23 \times \sqrt{3}$  herringbone reconstruction [43]. For the photoemission experiments, the sample was illuminated with He-I radiation (photon energy  $h\nu=21.21$  eV) from a commercial UVS-300 light source (Specs GmbH) under an angle of incidence of 21° with respect to the surface plane. In order to increase the photon flux at the sample, the photon beam was focused by an ellipsoidal capillary down to a spot size of about 1200  $\mu\text{m}$  FWHM. During the photoemission measurements, the sample was cooled by liquid helium.

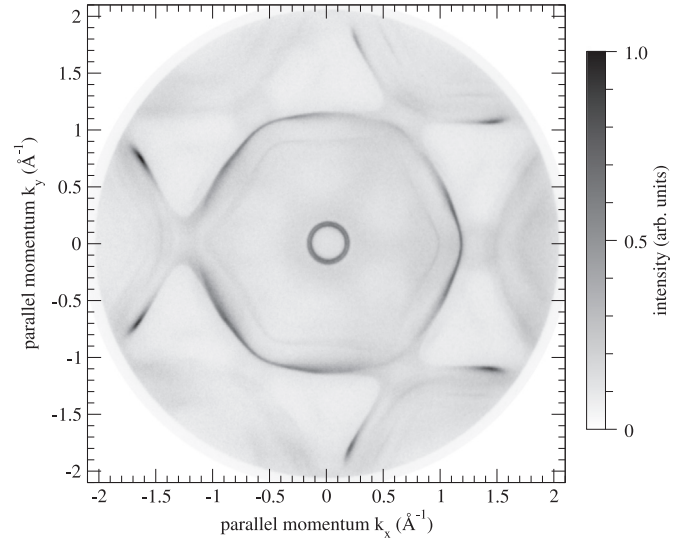


**Fig. 3.** Photoemission pattern from the Au(111) surface at the Fermi energy, measured with He-I ( $h\nu=21.22$  eV) radiation at an analyzer pass energy of 50 eV. Intensities are displayed on a linear gray scale.

We first discuss the results obtained from the spin integrated measurements of the clean Au(111) surface. Fig. 3 shows the distribution of photoelectrons, measured with He-I radiation at the Fermi energy. Data was integrated for a total of 25 min using a pass energy of  $E_{\text{pass}}=50$  eV and an analyzer slit of 0.2 mm, corresponding to a nominal energy resolution of 33 meV. The  $x$ - and  $y$ -coordinates of the image directly correspond to the parallel momentum coordinates (see Eq. (1)). We emphasize that Fig. 3 displays the image as recorded by the CCD camera of the direct detector arm, only corrected for the dark current of the CCD and the flat field image of the multi channel plate. No distortion correction and no symmetrization were applied.

At the Fermi energy, the maximum parallel momentum is given by Eq. (1) and  $E_{\text{max}} = h\nu - \Phi_S$ , with the known photon energy  $h\nu=21.21$  eV and the workfunction  $\Phi_S = 5.31$  eV of the Au(111) surface. At the Fermi energy, this results in a radius of the photoemission image of  $2.04 \text{\AA}^{-1}$ . As this cut-off momentum always has the dispersion of the free electron in the vacuum, the radius of the  $k_{\parallel}$  image provides an intrinsic calibration of the  $k_{\parallel}$  scale, in each measurement.

The experimental energy resolution was measured by taking a series of constant energy images across the Fermi edge, with an energy spacing of 5 meV. At the lowest sample temperature, 18 K, the Fermi-Dirac distribution leads to the broadening of the Fermi edge by an approximately Gaussian profile with 6.2 meV full width at half maximum. For each image, the integrated intensity of the Au(111) Shockley surface state, in the center of Fig. 3, was evaluated. Fig. 4 shows the measured intensity profiles as a function of binding energy for pass energies 100 eV, 50 eV, 30 eV, and 15 eV. The measured intensity profiles were normalized to a step height of 1, and shifted vertically for clarity. Lines in the figure show the fit to a Gaussian error function. For all measurements, a size of 0.2 mm for the energy defining slits of the HDA was selected.

Table 2 summarizes the energy resolution for various pass energies. Here,  $\Delta E_{\text{ideal}} = (d/2r_0)E_{\text{pass}}$  is the nominal energy resolution from the geometric consideration of the slit size,  $d$ , and the radius,  $r_0$ , of the hemisphere [23]. The best expected resolution, 10.0 meV at  $E_{\text{pass}} = 15$  eV, shows that the thermal broadening of the Fermi edge of  $w_F = 6.2$  meV cannot be neglected. Therefore, we correct the experimental width (FWHM) from the fit,  $w_{\text{fit}}$ , by  $\Delta E_{\text{exp}} = \sqrt{w_{\text{fit}}^2 - w_F^2}$ . The energy resolution obtained from the experiment, listed in Table 2, in general is in good agreement with

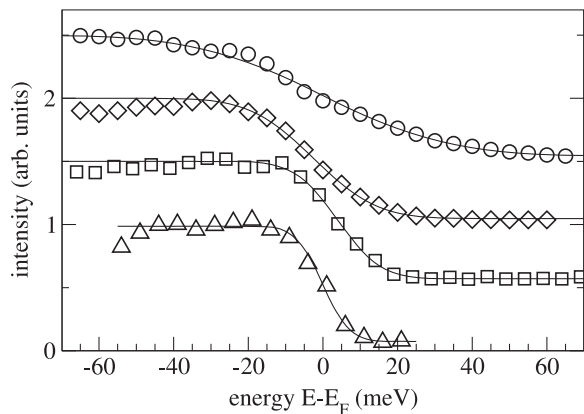


**Fig. 4.** Measured intensity (symbols) of the Shockley surface state as a function of binding energy at a sample temperature of  $T=18$  K. Curves for  $E_{\text{pass}}=100$  eV ( $\circ$ ),  $E_{\text{pass}}=50$  eV ( $\diamond$ ),  $E_{\text{pass}}=30$  eV ( $\square$ ),  $E_{\text{pass}}=15$  eV ( $\triangle$ ) are shifted vertically. Solid lines show a fit by a Gaussian error function (see Table 2).

**Table 2**

Nominal ( $\Delta E_{\text{ideal}}$ ) and measured ( $\Delta E_{\text{exp}}$ ) energy resolution for 0.2 mm analyzer slits, obtained from the fit of a Gaussian error function to the experimental intensity profiles in Fig. 4.

$E_{\text{pass}}$	$\Delta E_{\text{ideal}}$ (meV)	$\Delta E_{\text{exp}}$ (meV)
100	66.67	$56.9 \pm 4.0$
50	33.33	$30.2 \pm 1.9$
30	20.00	$20.1 \pm 3.1$
15	10.00	$11.9 \pm 1.8$

the nominal value. For the pass energies of 30 eV and above, we find the energy resolution equal, or slightly better than the expected value. For the lowest pass energy used, 15 eV, we find  $\Delta E = 12$  meV, i.e. 20% larger than the purely geometric expectation. We assume that this additional broadening can be attributed to the stability of the energy defining voltage supplies, which was measured to be better than 5 mV peak-to-peak, and residual magnetic fields.

The Shockley surface state of Au(111) exhibits a Rashba-type splitting into two spin sub-bands due to spin-orbit interaction [14,15]. In the two-dimensional Fermi-surface contour this manifests itself in two concentric circular bands with opposite spin, which are separated by  $\Delta k_{\parallel} = 0.025 \text{ \AA}^{-1}$ . We observe this splitting of the surface state already in the full image of the surface Brillouin zone in Fig. 3. A better resolved quantitative measurement of the spectral width of the Au(111) surface state is obtained by electron optically selecting a larger magnification of the momentum image. Fig. 5a is measured with a pass energy of 30 eV, corresponding to an energy resolution of 20 meV (see Table 2). The two concentric rings of the surface state are clearly separated, where the intensity in between the inner and the outer state nearly reduces to the background level.

The dispersion of the Au(111) surface state was measured by acquiring a series of momentum images at several kinetic energies with steps of 10 meV. From this three-dimensional data set ( $k_x$ ,  $k_y$ ,  $E$ ), sections along arbitrary directions can be selected. Fig. 5b shows a section along the  $\bar{M} - \bar{\Gamma} - \bar{M}$  direction, i.e. along the horizontal line with  $k_y=0$ , containing a total of 63 energy slices measured within 120 min. In agreement with the Rashba model we find the two nearly free-electron parabolas (experimentally determined effective mass  $m^*/m_e = 0.250$ ). A quantitative analysis of the measured peak positions and line shape is shown in Fig. 5c. The measured intensity profile along the horizontal line ( $k_y=0$ ) at the Fermi energy consists of four peaks, in total.

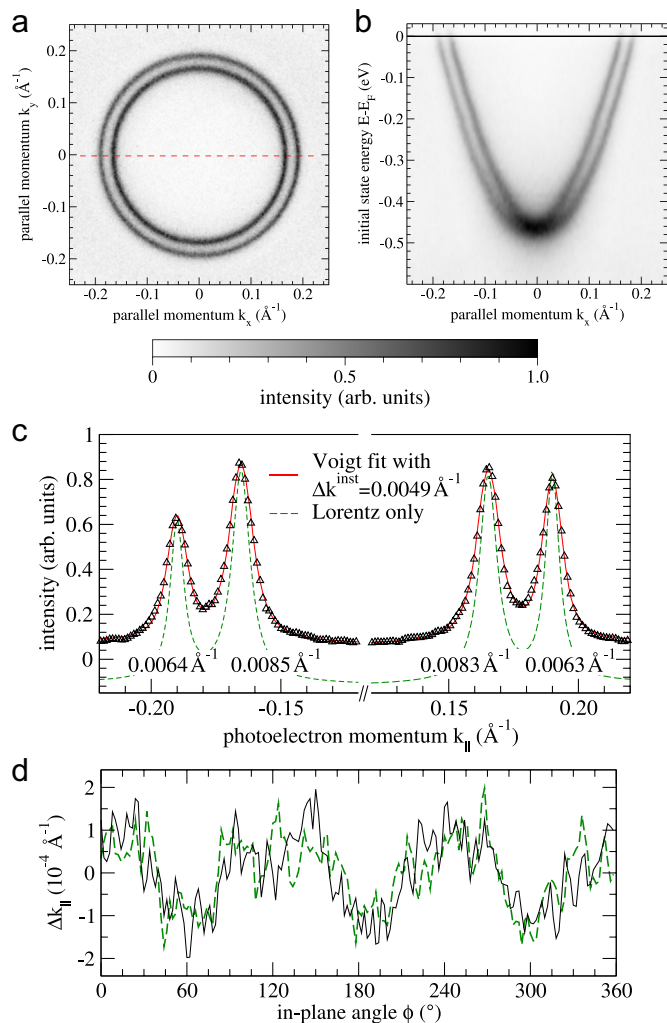


**Fig. 5.** (a) Detail of the Rashba-split Shockley surface state ( $E = E_F$ ), recorded at pass energy 30 eV and using a higher momentum magnification. (b) Dispersion of the surface state obtained by a horizontal ( $k_y=0$ ) cut through the data of (a) measured at different energies. (c) Intensity profile at  $k_y=0$  with a fit (solid line) to a Voigt line shape with  $0.005 \text{ \AA}^{-1}$  (FWHM) Gaussian broadening and the Lorentzian contribution (dashed line). Numbers indicate the Lorentzian width. (d) Deviation  $\Delta k_{\parallel}$  of the radius from an ideal circular shape of the outer (solid line) and the inner (dashed line) ring.

The measured intensities can be well fitted by double Voigt profiles on the left and right side, respectively, including a linear background. The fitted peak positions yield a  $k_{\parallel}$  diameter of the outer and inner ring of  $\pm 0.190 \text{ \AA}^{-1}$  and  $\pm 0.165 \text{ \AA}^{-1}$ , respectively. The measured separation on the in-plane momentum axis thus is  $\Delta k_{\parallel} = 0.025 \text{ \AA}^{-1}$ , in good agreement with other results [12,13]. The instrumental momentum resolution is considerably better than the observed line width of the surface state and is included by a common Gauss width parameter for all peaks. The best fit is obtained for an instrumental broadening of

$$\Delta k_{\parallel}^{\text{instr}} = 0.0049 \text{ \AA}^{-1} \quad (5)$$

full width at half maximum (FWHM). This  $k_{\parallel}$  resolution is about one order of magnitude better than values obtained with a momentum imaging photoelectron microscope, previously [29].

The Lorentzian line shape observed in photoemission peaks is generally related to the finite lifetime of the initial and final states involved in the photoemission process [44,45]. The fit shown in Fig. 5c (dashed line) reveals a different Lorentzian width  $\Gamma$

(FWHM) of the outer and the inner ring. We find consistently on both sides that the outer surface state ring ( $r_{\text{outer}}=0.0064 \text{ \AA}^{-1}$ ) is 25% narrower than the inner ring ( $r_{\text{inner}}=0.0085 \text{ \AA}^{-1}$ ). As we measure the width along the  $k_{\parallel}$ -axis, the more meaningful lifetime energy broadening is obtained through the dispersion of the respective band ( $n$ ) at the intersection with the measured energy slice

$$\Delta E_n = r_n \cdot \left[ \frac{\partial E_n}{\partial k_{\parallel}} + \frac{\partial E_n}{\partial k_{\perp}} \frac{\partial k_{\perp}}{\partial k_{\parallel}} \right] \quad (6)$$

As the two-dimensional surface state has no explicit dependence on the  $z$ -momentum coordinate, the second term in Eq. (6) including the unknown final state dispersion ( $k_{\perp}^f$ ) vanishes [44]. As both parabola branches of the surface state are separated by a constant parallel momentum, the derivative of the dispersion relation at the Fermi energy has the same value for the inner and the outer peak and affects both line widths in the same way. From this, we obtain a value of  $\Delta E_{\text{outer}} = 34 \text{ meV}$  and  $\Delta E_{\text{inner}} = 46 \text{ meV}$  for the lifetime related energy broadening of the outer and the inner ring of the surface state at the Fermi energy.

The lifetime related line width measured in photoemission contains, in general, contributions from scattering channels due to electron–electron, electron–phonon, and electron–defect interaction. The separation of the contributions usually involves assumptions about their functional dependence. For instance, the electron–electron scattering related broadening for the Shockley surface states on the noble metals was found to monotonically increase with binding energy, being negligible at the Fermi level [46–48]. The spectral line width is usually studied at the  $\bar{\Gamma}$  point, neglecting a possible  $k_{\parallel}$  dependence. The latter is also not expected in the case of the Au(111) surface, within the Rashba model [49]. In contrast to our result, photoemission measurements in Ref. [49] did not show significantly different line widths of the inner and the outer ring of the Au(111) surface state at the Fermi energy. However, line widths were about a factor of two larger compared to the present results, possibly related to the surface quality of the sample or  $k_{\parallel}$  resolution.

#### 4. Non-circularity of the surface state

Visual inspection of the Fermi surface contour in Fig. 5a shows a perfectly circular shape of the surface state. For the Shockley surface states on the [111] *fcc* surfaces, the prototype of a two-dimensional nearly free electron gas, this is the expected result. On the close packed surfaces, the corrugation of the electron density is smeared out and an in-plane gradient of the potential becomes negligible. The surface state then can be effectively described by an isotropic parabolic dispersion of a free electron only characterized by a modified effective mass  $m^*/m_e \neq 1$ . This is not the case when a considerable in-plane gradient of the potential is present, for instance for various surface alloys like Bi/Cu(111) or Bi/Ag(111), where the six-fold rotational symmetry of the surface layer is clearly observed in the Fermi surface contour [31,50,51].

A precise measurement of the rotational symmetry of the Shockley surface state by conventional ARPES using scanning the sample or analyzer is complicated by the mechanical movement involved. By contrast, the present momentum microscope acquires the complete Fermi surface contour simultaneously. Fig. 5d shows the measured radius of the outer (solid line) and inner (dashed line) ring of the surface state, obtained from the center positions of the Voigt profile fit, respectively. The in-plane angle is measured with respect to the horizontal  $\bar{\Gamma} - \bar{M}$  direction. We find a non-circularity of both surface state rings with an amplitude of

$\Delta k_{\parallel} \approx 0.3 \cdot 10^{-3} \text{ \AA}^{-1}$  peak-to-peak, and a threefold  $120^\circ$  periodicity. An estimate of the statistical uncertainty of the radius measurement is given by the scatter of individual data points and the agreement between the inner and the outer surface state ring. Here, this uncertainty is of the order  $\leq 0.1 \cdot 10^{-3} \text{ \AA}^{-1}$  peak-to-peak, and clearly distinguished from the observed three-fold modulation.

Instrumental distortions can be excluded as the source of the three-fold radial symmetry for several reasons: first, the electron optical system does not contain elements with a three-fold symmetry. The major breaking of the rotational symmetry is introduced by the energy filter, which however might give rise to a two-fold astigmatism along the  $k_y$  axis. Such contributions can be clearly separated from the observed three-fold periodicity. More importantly, we additionally checked that the three-fold periodicity of the surface state radius is aligned with the crystal axes of the sample. For this, the Au(111) sample was mechanically rotated, while all other parameters of the instrument were left unchanged. We found that this rotation leads to a corresponding phase shift in  $\Delta k_{\parallel}(\phi)$ .

We conclude that the variation of the in-plane momentum follows the three-fold bulk symmetry. A six-fold symmetry from the surface layer, as outlined above, is not clearly observed, but might be present below the noise level. We therefore relate the observed deviation from a perfect circle to the interaction between the surface state and the edge of the projected bulk band gap. Previously, a deviation from the free-electron description due to hybridization with bulk states could only be observed experimentally when the surface state of Cu(111) approaches the edge of the band gap above the Fermi level [52]. A similar behavior was also predicted for Au(111) [21]. At the Fermi level, however, the deviation from the free-electron gas becomes small, in general. Our results provide a quantitative estimation for limits of an isotropic free electron model of the Shockley surface state, for the first time.

#### 5. Spin resolved results

Spin resolved photoelectron momentum distributions were recorded by introducing a spin polarizing electron mirror into the electron optical path after the energy filter. The principle of spin filtering of a two-dimensional electron distribution was introduced earlier using a W(100) scattering target [32]. Spin contrast is obtained due to the spin dependent reflectivity of low-energy electrons at the non-magnetic surface of the scattering target which is governed by spin–orbit coupling, such that electrons with opposite spin see different scattering potentials, leading to different scattering amplitudes [53]. Image information is transmitted in the momentum conserving (0 0) LEED beam. Previous measurements showed that scattering energies of 26.5 eV and 30.5 eV with a spin sensitivity of 42% and 5%, respectively, are efficient working points for a clean W(100) scattering target [32,33]. Using an Ir(100) single crystal, a sharply peaked high spin asymmetry and reflectivity was found at scattering energies around 10 eV and a rather broad asymmetry maximum around 40 eV for the clean  $5 \times 1$  reconstructed surface [54]. For a pseudomorphic monolayer of Au on Ir(100), experimental data and theory from Ref. [34] also find an asymmetry maximum at 40 eV scattering energy under an angle of incidence of  $45^\circ$ , while the low energy region was not explored, so far. In addition, the reported long-term stability of the Au/Ir(100) surface of several weeks makes this system an interesting candidate for the imaging spin-filter of the present momentum microscope.

The clean Ir(100) crystal was prepared by repetitive heating to

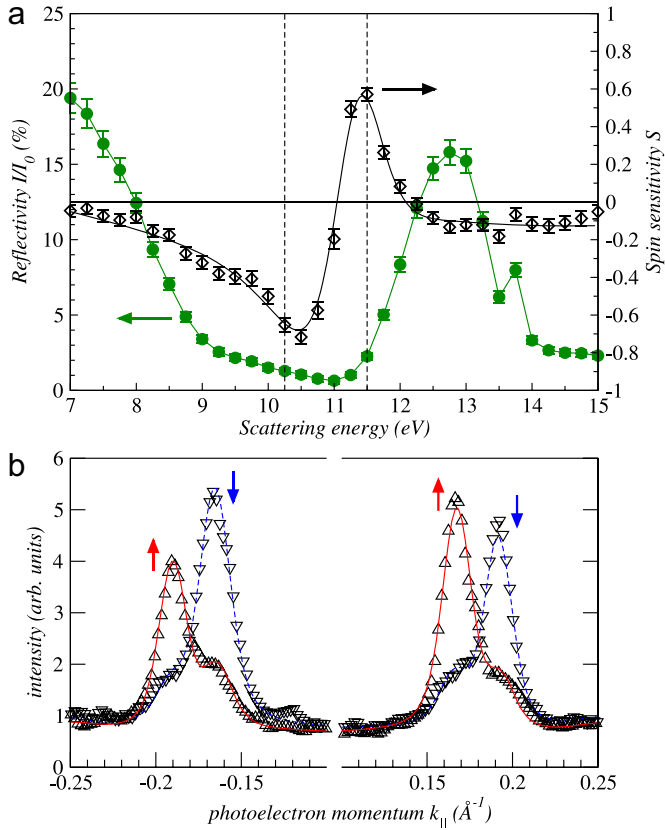


**Fig. 6.** (a) Spin averaged reflectivity ( $I/I_0$ , left), and spin sensitivity ( $S$ , right) as a function of the scattering energy. (b) Line profiles over the Au(111) surface state at  $k_y=0$  for  $E_{\text{scatt}} = 10.25$  eV ( $\nabla$ ) and  $E_{\text{scatt}} = 11.50$  eV ( $\triangle$ ) together with a model fit for  $S = -0.65$  and  $S = +0.57$ , respectively.

1400 K in an oxygen pressure of  $5 \cdot 10^{-8}$  mbar followed by high temperature heating to 1700 K under UHV conditions. The procedure was repeated until a carbon free surface showing the  $5 \times 1$  reconstruction was obtained [55]. Gold was deposited onto the clean Ir(100)- $5 \times 1$  surface followed by annealing cycles of 90 s duration after which an end temperature of 1140 K was reached, until the stable unreconstructed pseudomorphic monolayer was obtained [34].

Fig. 6a shows the reflectivity and asymmetry for scattering energies in the range from  $E_{\text{scatt}} = 7.0$  eV to  $E_{\text{scatt}} = 15.0$  eV, measured 2 days after the Au monolayer was prepared. The scattering energy was varied by the potential applied to the Au/Ir(100) crystal, while the electrode voltages of the retarding and accelerating lenses were adjusted such that the magnification of the momentum image in the  $90^\circ$  inclined detector arm was constant. The spin sensitivity,  $S$ , and reflectivity,  $R$ , were evaluated from horizontal intensity profiles taken across the Rashba split Au(111) surface state. Fig. 6b shows two intensity profiles recorded at a scattering energy of 10.25 eV and 11.50 eV. Intensities were normalized to the background level, for clarity. At 10.25 eV, in contrast to the spin integrated profile in Fig. 5c, only the right ( $\downarrow$ ) peak of the two spin sub-bands appears on both sides of the surface state ring. The situation gets reversed at 11.50 eV with strong left ( $\uparrow$ ) peaks, due to reversal of  $S$ .

In order to determine the value of  $S$  from the profiles, we follow a modified procedure as outlined in Ref. [56], and describe the primary photo current,  $i_0$ , and polarization,  $p_0$ , by a synthesized profile of the partial intensities of the spin-up ( $i_0^\uparrow$ ) and spin-down ( $i_0^\downarrow$ ) channels

$$i_0^\uparrow = \mathcal{V}_l^\uparrow + \mathcal{V}_r^\uparrow + \frac{1}{2}\mathcal{BG}, \quad i_0^\downarrow = \mathcal{V}_l^\downarrow + \mathcal{V}_r^\downarrow + \frac{1}{2}\mathcal{BG} \quad (7)$$

$$i_0 = i_0^\uparrow + i_0^\downarrow, \quad p_0 = \frac{i_0^\uparrow - i_0^\downarrow}{i_0^\uparrow + i_0^\downarrow} \quad (8)$$

Here,  $\mathcal{V}_{l,r}^{\uparrow,\downarrow}$  is the Voigt profile obtained from the fit in Fig. 5c for the spin-up ( $\uparrow$ ) or -down ( $\downarrow$ ) peaks on the left ( $l$ ) or right ( $r$ ) side of the surface state ring, and  $\mathcal{BG}$  is the non-polarized background function. The scattered intensities then can be written by [57]

$$i_s = [i_0 \cdot (1 + p_0 \cdot S) \cdot R] \cdot \mathcal{G}, \quad (9)$$

where  $S$  and  $R$  are scalar fit parameters for the spin-sensitivity and the reflectivity, respectively.

The result of the fit is displayed by the dashed (10.25 eV) and solid (11.50 eV) lines in Fig. 6b. The best fit was obtained with  $S = -0.65$  and  $R = 1.3\%$  for 10.25 eV, and  $S = +0.57$  and  $R = 2.3\%$  for 11.50 eV. The absolute scale of the reflectivity was calibrated by comparing the single-electron count rates on the direct and spin-filtered detectors. Convolution by the gaussian function,  $\mathcal{G}$ , accounts for the reduced image resolution introduced by reflection at the spin-filter target, where the best fit was obtained with a  $\text{FWHM} = 0.011 \text{ \AA}^{-1}$ . Given the complete field-of-view of the spin-filtered image was a circle  $0.90 \text{ \AA}^{-1}$  in diameter, this corresponds to 80 diagonal points and about  $N = 5000$  points in the circular field-of-view. For comparing the detection efficiency, we previously introduced the two-dimensional figure-of-merit,  $\mathcal{F}_{2D} = R \cdot S^2 \cdot N$ , where a value of  $\mathcal{F}_{2D} = 8$  was found for the 26.5 eV working point of W(100) [32,33]. Using the values given above for Au/Ir(100), we find even a considerably higher efficiency of  $\mathcal{F}_{2D} = 28$  and  $\mathcal{F}_{2D} = 37$  for the two working points at  $E_s = 10.25$  eV and 11.50 eV, respectively.

Spin-resolved photoelectron momentum maps of the Au(111) surface state were measured by recording images at the working points with negative and positive spin sensitivity at  $E_{\text{scatt}} = 10.25$  eV and  $E_{\text{scatt}} = 11.50$  eV. As shown in the horizontal profiles in Fig. 6b, each of the scattering energies contains a major contribution from the spin-up (11.50 eV) or the spin-down (10.25 eV) spin channel. The reason for this simple interpretation is that the spin-sensitivity is almost directly opposite ( $-65\%$  and  $+57\%$ ) at these working points. In general, from the measurement with two different spin sensitivities,  $S_l$  and  $S_h$ , the spin-polarization  $P(x, y)$ , and analogous the spin-averaged intensity  $I_0(x, y)$ , at each pixel, is derived according to the procedure outlined in Ref. [33]

$$P(x, y) = \frac{\mathcal{I}_l(x, y) - \mathcal{I}_h(x, y)}{S_l \cdot \mathcal{I}_h(x, y) - S_h \cdot \mathcal{I}_l(x, y)} \quad (10)$$

$$I_0(x, y) = \frac{S_l \mathcal{I}_h(x, y) - S_h \mathcal{I}_l(x, y)}{S_l - S_h}, \quad (11)$$

where  $\mathcal{I}_{l,h} = I_{l,h}/R_{l,h}$  is the measured intensity image  $I_{l,h}$  normalized to the reflectivity reference image  $R_{l,h}$  for the low ( $l$ ) or high ( $h$ ) scattering energy [33]. As in Eq. (8) the same information also can be represented by the partial intensities of the spin-up ( $\uparrow$ ) and spin-down ( $\downarrow$ ) channels. Using the spin sensitivities derived above, these partial intensities for the Au(111) surface state at the Fermi energy are displayed in Fig. 7a and b. Here, maximum intensity in each spin channel is obtained on the horizontal axis at  $k_y = 0$ , where only the spin-up or spin-down component is visible in one image, indicating clear separation of spin channels.

While all data presented up to here was measured using unpolarized He-I radiation, for comparison we also performed measurements using 6.05 eV photons from the 4th harmonic of a Ti:Sa oscillator ( $\Delta h\nu \approx 10$  meV, 80 MHz repetition rate). The result

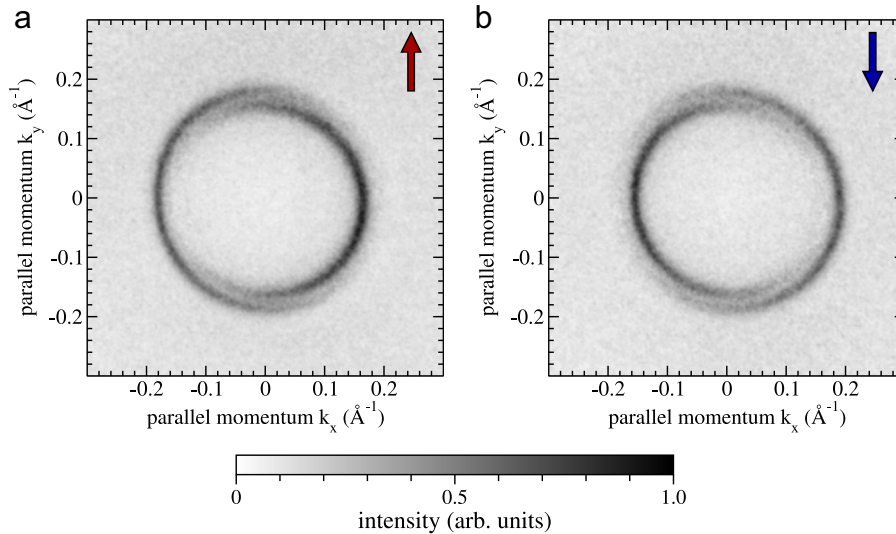


**Fig. 7.** (a) Partial photoemission intensity map for the spin-up component measured with He-I radiation. On the horizontal axis, only one ring of the surface state is observed. (b) The same for the spin-down component.

for p-polarized light is shown in Fig. 8a as the combined map of vertical spin polarization  $P_y$  and intensity  $I_0$  at the Fermi energy. As outlined in Fig. 8d, the blue-red color corresponds to the value of the spin polarization, and the saturation corresponds to the intensity. The inner and the outer ring are clearly distinguished by their opposite polarization, where on the left half of the image the outer (inner) ring polarization is positive (negative), and vice versa on the right half. This is a consequence of the circular spin texture [14,15], outlined in Fig. 8c. In consequence, the polarization vanishes on vertical axis ( $k_x=0$ ) when the spin is always aligned normal to  $\vec{k}$  as in the Rashba model. This is in direct agreement with Fig. 8a, and also with the partial intensities displayed in Fig. 7.

Fig. 8b shows the spin resolved dispersion of the surface state along the  $x$ -axis. As for the spin-averaged experiments before, this section is obtained from a series of constant energy slices like in Fig. 8a. For the spin resolved experiment, images at both scattering energies were recorded in steps of 25 meV initial state energy. The total acquisition time for one spin resolved energy slice was 480 s. The spin information allows a clear separation between two free-electron like parabolic dispersions with spin-up and spin-down polarization shifted to the negative and the positive direction on the momentum axis, respectively. We find our results in perfect agreement with the Rashba model. Compared to previous lower-resolution studies of this system [58,16], the spin splitting of the two free electron like parabola branches is directly resolved in the spin-resolved experiment, and allows a quantitative comparison with theoretical models.

Fig. 8e shows line profiles of the vertical polarization component  $P_y$  along the  $x$ -axis ( $k_y=0$ ). For all experiments, the polarization has a sharp plus-minus structure at the location of the outer and inner ring, and drops rapidly to zero outside of the surface state. The highest absolute polarization value is observed for the p-polarized laser excitation, with peak values of about  $\pm 80\%$ . The polarization in the area enclosed by the surface state does not drop completely to zero, which can be understood by the background photoemission intensity being extremely low, due to the absence of initial states inside the L-gap. As a consequence, the tails of the Lorentzian peaks considerably contribute to the spin polarization. We note that this qualitatively resembles the theoretical shape of the polarization profile [14]. For s-polarized laser excitation, the maximum polarization value is reduced to about  $\pm 40\%$ . The reason is the low photoemission intensity from the surface state due to the sp-like orbital symmetry, relative to the

background. The profile for 21.21 eV is very similar to the profile observed with the p-polarized laser, while a reduced peak polarization is due to the additional background from helium satellite lines. In general, we find a very good agreement between the measurements with different photon energies and light polarizations. A pronounced dependence on the photon energy and polarization is not observed in our experiments, while this might be different when other photoemission geometries are considered [14].

## 6. Summary

We presented a momentum microscope for the high resolution measurement of electronic band structures with full two-dimensional spin information. The high efficiency of the simultaneous measurement of the photo current emitted into the full solid angle above a sample surface is a fundamental advantage of a momentum microscope. Unlike previous PEEM based instruments, the instrument presented here is optimized for the requirements of bandstructure imaging with high resolution.

We demonstrated an energy resolution of 12 meV, measured at the Fermi edge of the helium-cooled Au(111) sample. The instrumental momentum resolution of  $0.0049 \text{ \AA}^{-1}$  that was obtained from the Gaussian broadening of line profiles across the Shockley surface state is among the best values reported in state-of-the-art ARPES experiments [49,59]. Moreover, we demonstrated a considerably higher accuracy for the relative measurement of the radius of the "circular" ring of the nearly-free-electron like surface state. We find a three-fold periodicity in the order of  $\Delta k_{\parallel} = 3 \cdot 10^{-4} \text{ \AA}^{-1}$ . Deviations from the ideal free-electron model can be expected due to the interaction with bulk bands, which was proven before only above the Fermi level where the distance to the band edge is much smaller.

Using a pseudomorphic monolayer of Au on Ir(100), the imaging spin-filter is characterized by a long-term stability of several weeks [34]. At low scattering energies around 11 eV we found sharply peaked working points with reversed spin sensitivity that are ideally suited for the acquisition of monochromatic momentum images. Compared to previous work using a W(100) target we find a significant increase of the 2D detection efficiency, related to a high, and reversible, spin sensitivity of about  $\pm 60\%$ .

The spatially resolved measurement of the bandstructure is an

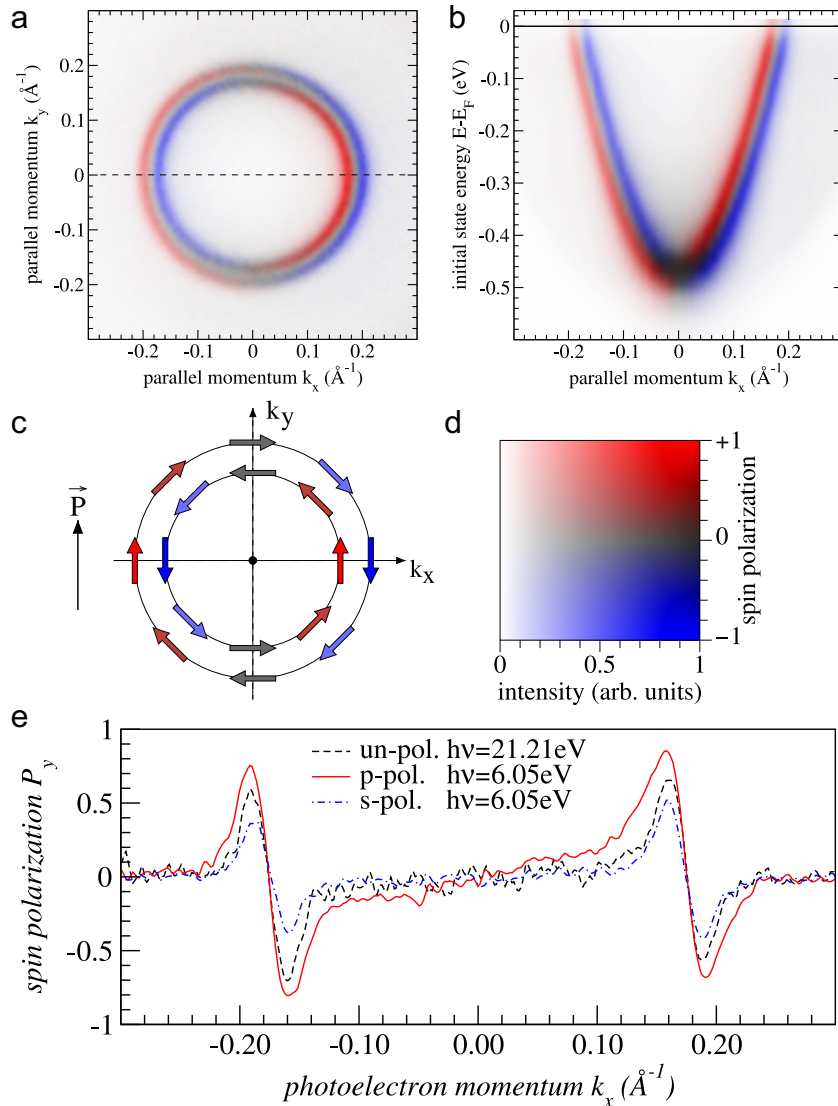


**Fig. 8.** (a) Measured spin polarization and intensity map at  $E_F$  of the Au(111) surface state excited by p-polarized 6.05 eV photons. The 2D color code is displayed in (d). (b) Spin resolved dispersion along the horizontal ( $k_y=0$ ) axis. (c) Schematic model of the spin texture of the Rashba surface state. Arrows indicate the spin direction, the color corresponds to the observed projection on the quantization axis  $\vec{P}$ . (e) Profile of  $P_y$  along  $k_x$  for measurements with He-I radiation and s- and p-polarized 6.05 eV light.

intrinsic property of the momentum microscope. The analyzed area is determined by the effective size of the analyzer slit, or can be confined further by an aperture in the first spatial image plane to a dimension only limited by the aberration of the objective lens. For instance, a momentum-image covering  $\pm 1 \text{ \AA}^{-1}$  can be collected from an area as small as  $1 \mu\text{m}$  (see Fig. 2b). The spatial resolution for bandstructure imaging still could be improved by further reduction of the spherical aberration of the cathode lens. An interesting prospect is the combination with aberration correction schemes established in electron microscopy [60]. In particular, using electrostatic mirrors the correction up to the third order was demonstrated recently for photoemission- and low-energy electron microscopy [61,62]. We expect that such improvements will enable the measurement of the electronic structure of sub-micrometer sized objects.

The  $k_{\parallel}$  imaging principle of the momentum microscope is not strictly limited to the exact type of HDA energy filter used here. In general, the acquisition of two-dimensional momentum image slices requires an energy filter that preserves the image information of the electron ensemble. While the chosen setup of two HDAs is one of the simplest geometries to fulfill this requirement,

several alternative dispersive filters with appropriate multiple-focussing properties exist [63,64]. Moreover, using pulsed light sources like a laser or a synchrotron beam, the energy slice could be selected by the time-of-flight (ToF) of the electrons in a low-energy drift tube [65] replacing the dispersive filter. We are currently investigating the parallel acquisition of multiple energy slices by such a ToF analyzer, which is especially advantageous when spin resolution shall be combined with highest energy resolution.

## Acknowledgments

We would like to thank F. Thiele and D. Hartung (MPI-Halle) for their assistance during the construction and installation of the momentum microscope.

## References

- [1] F. Reinert, S. Hüfner, *New J. Phys.* 7 (2005) 97–97.
- [2] A. Damascelli, Z.-X. Shen, *Rev. Mod. Phys.* 75 (2003) 473–541.

- [3] X. Zhou, G. Liu, J. Meng, W. Zhang, H. Liu, L. Zhao, X. Jia, *Physica Status Solidi (a)* (2010) 2674–2692.
- [4] P. Richard, T. Sato, K. Nakayama, T. Takahashi, H. Ding, *Rep. Prog. Phys.* 74 (2011) 124512.
- [5] M. Bianchi, D. Guan, S. Bao, J. Mi, B.B. Iversen, P.D. King, P. Hofmann, *Nat Commun.* 1 (2010) 128.
- [6] D. Hsieh, Y. Xia, D. Qian, L. Wray, J.H. Dil, F. Meier, J. Osterwalder, L. Patthey, J. G. Checkelsky, N.P. Ong, A.V. Fedorov, H. Lin, A. Bansil, D. Grauer, Y.S. Hor, R. J. Cava, M.Z. Hasan, *Nature* 460 (2009) 1101–1105.
- [7] S. Suga, K. Sakamoto, T. Okuda, K. Miyamoto, K. Kuroda, A. Sekiyama, J. Yamaguchi, H. Fujiwara, A. Irizawa, T. Ito, et al., *J. Phys. Soc. Jpn.* 83 (2014) 014705.
- [8] J. Kirschner, R. Feder, J.F. Wendelken, *Phys. Rev. Lett.* 47 (1981) 614–617.
- [9] A. Eyers, F. Schäfers, G. Schönhense, U. Heinzmann, H.P. Oepen, K. Hünlich, J. Kirschner, G. Borstel, *Phys. Rev. Lett.* 52 (1984) 1559–1562.
- [10] R. Raue, H. Hopster, R. Clauberg, *Phys. Rev. Lett.* 50 (1983) 1623–1626.
- [11] S. LaShell, B.A. McDougall, E. Jensen, *Phys. Rev. Lett.* 77 (1996) 3419–3422.
- [12] F. Reinert, G. Nicolay, S. Schmidt, D. Ehm, S. Hüfner, *Phys. Rev. B* 63 (2001) 115415.
- [13] F. Reinert, *J. Phys.: Condens. Matter* 15 (2003) S693.
- [14] J. Henk, A. Ernst, P. Bruno, *Phys. Rev. B* 68 (2003) 165416.
- [15] J. Henk, M. Hoesch, J. Osterwalder, A. Ernst, P. Bruno, *J. Phys.: Condens. Matter* 16 (2004) 7581.
- [16] J. Osterwalder, in: *Lecture Notes in Physics*, vol. 697, 2006, pp. 95–120.
- [17] C.M. Cacho, S. Vlaic, M. Malvestuto, B. Ressel, E.A. Seddon, F. Parmigiani, *Rev. Sci. Instrum.* 80 (2009) 043904.
- [18] C. Jozwiak, J. Graf, G. Lebedev, N. Andresen, A.K. Schmid, A.V. Fedorov, F. El Gabaly, W. Wan, A. Lanzara, Z. Hussain, *Rev. Sci. Instrum.* 81 (2010) 053904.
- [19] C. Jozwiak, C.-H. Park, K. Gotlieb, C. Hwang, D.-H. Lee, S.G. Louie, J.D. Denlinger, C.R. Rotundu, R.J. Birgeneau, Z. Hussain, et al., *Nat. Phys.* 9 (2013) 293–298.
- [20] Z. Xie, S. He, C. Chen, Y. Feng, H. Yi, A. Liang, L. Zhao, D. Mou, J. He, Y. Peng, et al., *Nat. Commun.* 5 (2014) 3382.
- [21] J. Ibañez Azpiroz, A. Bergara, E.Y. Sherman, A. Eiguren, *Phys. Rev. B* 88 (2013) 125404.
- [22] S.N.P. Wissing, C. Eibl, A. Zumbülte, A.B. Schmidt, J. Braun, J. Minár, H. Ebert, M. Donath, *New J. Phys.* 15 (2013) 105001.
- [23] F. Hadjarab, J.L. Erskine, *J. Electron. Spectrosc. Relat. Phenom.* 36 (1985) 227–243.
- [24] D. Pierce, R. Celotta, M. Kelley, J. Unguris, *Nucl. Instrum. Methods Phys. Res. Sect. A: Accel. Spectrom. Detect. Assoc. Equip.* 266 (1988) 550–559.
- [25] A. Winkelmann, D. Hartung, H. Engelhard, C.-T. Chiang, J. Kirschner, *Rev. Sci. Instrum.* 79 (2008) 083303.
- [26] T. Okuda, K. Miyamaoto, H. Miyahara, K. Kuroda, A. Kimura, H. Namatame, M. Taniguchi, *Rev. Sci. Instrum.* 82 (2011) 103302.
- [27] M. Kolbe, P. Lushchik, B. Peteret, H.J. Elmers, G. Schönhense, A. Oelsner, C. Tusche, J. Kirschner, *Phys. Rev. Lett.* 107 (2011) 207601.
- [28] M. Kotsugi, W. Kuch, F. Offi, L.I. Chelaru, J. Kirschner, *Rev. Sci. Instrum.* 74 (2003) 2754–2758.
- [29] B. Krömker, M. Escher, D. Funnemann, D. Hartung, H. Engelhard, J. Kirschner, *Rev. Sci. Instrum.* 79 (2008) 053702.
- [30] A. Winkelmann, C. Tusche, A.A. Ünal, M. Ellguth, J. Henk, J. Kirschner, *New J. Phys.* 14 (2012) 043009.
- [31] A.A. Ünal, A. Winkelmann, C. Tusche, F. Bisio, M. Ellguth, C.-T. Chiang, J. Henk, J. Kirschner, *Phys. Rev. B* 86 (2012) 125447.
- [32] C. Tusche, M. Ellguth, A.A. Ünal, C.-T. Chiang, A. Winkelmann, A. Krasnyuk, M. Hahn, G. Schönhense, J. Kirschner, *Appl. Phys. Lett.* 99 (2011) 032505.
- [33] C. Tusche, M. Ellguth, A. Krasnyuk, A. Winkelmann, D. Kutnyakhov, P. Lushchik, K. Medjanik, G. Schönhense, J. Kirschner, *Ultramicroscopy* 130 (2013) 70–76.
- [34] J. Kirschner, F. Giebels, H. Gollisch, R. Feder, *Phys. Rev. B* 88 (2013) 125419.
- [35] M.J. Pellin, C.E. Young, D.M. Gruen, *Scanning Microsc.* 2 (1988) 1353.
- [36] M. Escher, N. Weber, M. Merkel, C. Ziethen, P. Bernhard, G. Schönhense, S. Schmidt, F. Forster, F. Reinert, B. Krömker, D. Funnemann, *J. Phys.: Condens. Matter* 17 (2005) S1329–S1338.
- [37] D. Funnemann, M. Escher, *Patent EP 1 559 126 B1*.
- [38] D.A. Dahl, *Int. J. Mass Spectrom.* 200 (2000) 3–25.
- [39] M. Bernheim, *Eur. Phys. J. Appl. Phys.* 36 (2006) 193–204.
- [40] E. Bauer, *Ultramicroscopy* 17 (1985) 51–56.
- [41] P.W. Hawkes, *J. Phys. D: Appl. Phys.* 1 (1968) 131.
- [42] R. Tromp, *Ultramicroscopy* 111 (2011) 273–281.
- [43] M. Van Hove, R. Koestner, P. Stair, J. Bibrani, L. Kesmodel, I. Barto, G. Somorjai, *Surf. Sci.* 103 (1981) 189–217.
- [44] N.V. Smith, P. Thiry, Y. Petroff, *Phys. Rev. B* 47 (1993) 15476–15481.
- [45] J. Sánchez-Royo, J. Avila, V. Pérez-Dieste, M. Asensio, *Surf. Sci.* 482–485 (2001) 752–758.
- [46] T. Valla, A.V. Fedorov, P.D. Johnson, S.L. Hulbert, *Phys. Rev. Lett.* 83 (1999) 2085–2088.
- [47] J. Kliewer, R. Berndt, E.V. Chulkov, V.M. Silkin, P.M. Echenique, S. Crampin, *Science* 288 (2000) 1399–1402.
- [48] A. Eiguren, B. Hellsing, F. Reinert, G. Nicolay, E.V. Chulkov, V.M. Silkin, S. Hüfner, P.M. Echenique, *Phys. Rev. Lett.* 88 (2002) 066805.
- [49] I.A. Nechaev, M.F. Jensen, E.D.L. Rienks, V.M. Silkin, P.M. Echenique, E. V. Chulkov, P. Hofmann, *Phys. Rev. B* 80 (2009) 113402.
- [50] J. Prempfer, M. Trautmann, J. Henk, P. Bruno, *Phys. Rev. B* 76 (2007) 073310.
- [51] C.R. Ast, J. Henk, A. Ernst, L. Moreschini, M.C. Falub, D. Pacilé, P. Bruno, K. Kern, M. Griioni, *Phys. Rev. Lett.* 98 (2007) 186807.
- [52] A.A. Ünal, C. Tusche, S. Ouazi, S. Wedekind, C.-T. Chiang, A. Winkelmann, D. Sander, J. Henk, J. Kirschner, *Phys. Rev. B* 84 (2011) 073107.
- [53] J. Kirschner, R. Feder, *Phys. Rev. Lett.* 42 (1979) 1008–1011.
- [54] D. Kutnyakhov, P. Lushchik, A. Fognini, D. Perriard, M. Kolbe, K. Medjanik, E. Fedchenko, S. Nepjiko, H. Elmers, G. Salvatella, C. Stieger, R. Gort, T. Bähler, T. Michlmayer, Y. Acremann, A. Vaterlaus, F. Giebels, H. Gollisch, R. Feder, C. Tusche, A. Krasnyuk, J. Kirschner, G. Schönhense, *Ultramicroscopy* 130 (2013) 63–69.
- [55] K. Heinz, G. Schmidt, L. Hammer, K. Müller, *Phys. Rev. B* 32 (1985) 6214–6221.
- [56] F. Meier, J.H. Dil, J. Osterwalder, *New J. Phys.* 11 (2009) 125008.
- [57] J. Kessler, chapter 3, in: *Polarized Electrons*, 2 edition, Springer-Verlag, Berlin, Heidelberg, New York, Tokyo, 1985, ISBN: 0-387-15736-0.
- [58] M. Hoesch, M. Muntwiler, V.N. Petrov, M. Hengsberger, L. Patthey, M. Shi, M. Falub, T. Greber, J. Osterwalder, *Phys. Rev. B* 69 (2004) 241401.
- [59] A. Nuber, J. Braun, F. Forster, J. Minár, F. Reinert, H. Ebert, *Phys. Rev. B* 83 (2011) 165401.
- [60] M. Haider, S. Uhlemann, E. Schwan, H. Rose, B. Kabius, K. Urban, *Nature* 392 (1998) 768–769.
- [61] T. Schmidt, A. Sala, H. Marchetto, E. Umbach, H.-J. Freund, *Ultramicroscopy* 126 (2013) 23–32.
- [62] R. Tromp, J. Hannon, W. Wan, A. Berghaus, O. Schaff, *Ultramicroscopy* 127 (2013) 25–39.
- [63] W. Poschenrieder, *Int. J. Mass Spectrom. Ion Phys.* 6 (1971) 413–426.
- [64] M. Ishihara, M. Toyoda, T. Matsuo, *Int. J. Mass Spectrom.* 197 (2000) 179–189.
- [65] G. Schönhense, A. Oelsner, O. Schmidt, G. Fecher, V. Mergel, O. Jagutzki, H. Schmidt-Böcking, *Surf. Sci.* 480 (2001) 180–187.